Design and Finite Element Analysis of Flour Packaging Machine for Plantain Processing Plant

Emmanuel O. Olutomilola*, Sesan P. Ayodeji and Michael K. Adeyeri
Industrial and Production Engineering Department
Mechanical Engineering Department
Federal University of Technology
Akure, Ondo, Nigeria
eoolutomilola@futa.edu.ng

Date received: September 12, 2020
Revision accepted: May 6, 2021

Abstract

Plantain, the fourth most important crop, is crucial to food security and livelihoods of many people in Nigeria – the fifth leading plantain producer in the world. The demand for plantain flour is rapidly increasing due to its health benefits and industrial applications; hence, the need for more machines. However, importing flour-packaging machines is found to be not cost-effective. Thus, it is necessary to locally develop a flour packaging machine for a plantain flour production and packaging plant. For this reason, this paper aimed to present the design and finite element analysis of a flour packaging machine. The model was developed and after careful selection of suitable materials and design analysis, its functionality, structural integrity and design adequacy for fabrication were evaluated using SolidWorks 2016. The highest induced-stress and the lowest factor of safety values were obtained from the simulation of the machine's frame, which is made of mild steel. As evidenced by the simulation results, it was revealed that the machine will be able to serve its intended purpose. However, care must be taken to reinforce the locations with the highest induced-stress values on the machine, before or during fabrication, for optimum reliability.

***Keywords**: flour packaging machine, design, finite element analysis, plantain, processing plant*

1. Introduction

Diabetes is one of the leading causes of morbidity, debilitating diseases and death throughout the world (Oluwajuyitan and Ijarotimi, 2019; Hussain *et al*., 2020). Recently, it was reported that diabetes is a risk factor for coronavirus infectious disease 2019 (COVID-19) (Adeyeri *et al*., 2020; Seewoodhary and Oozageer, 2020). It is associated with increased incidence and severity of

COVID-19 (Singh *et al*., 2020) leading to high mortality (Hussain *et al*., 2020; Wang *et al*., 2020).

In Nigeria and some other parts of the world, plantain especially the unripe ones has been found to be very useful, effective and affordable in managing diabetes, treatment of anemia and liver disorders without negative side effects (Eleazu and Okafor, 2015; Olanrewaju and Abidemi, 2017; Olutomilola *et al.*, 2019; Olutomilola, 2021). Thus, managing or eliminating diabetes mellitus, which can also be done by consuming plantain and its associated products, is a promising way to weaken COVID-19 among diabetic patients (Olutomilola, 2021).

Globally, plantain is a crop that is crucial to food security and livelihoods of many people especially in Nigeria (Olutomilola and Omoaka, 2018). As a global commodity for food security, plantain has the potential to enhance food security (Kouame *et al*., 2017; Olutomilola, 2021). It was reported that after wheat, rice and corn, plantain is the fourth most important crop in the world (Alonso-Gomez *et al*., 2020; Olutomilola *et al.*, 2020). The demand for plantain flour is rapidly increasing due to the increased-awareness about its health or nutritional benefits and industrial applications (Fadimu *et al*., 2020). Therefore, there is a need to develop a plant for processing plantain into bagged-flour in Nigeria, being the largest producer of plantain in West Africa and fifth in the world (Ayodeji, 2016; Olutomilola, 2019). Essentially, plantain flour must be hygienically packaged in compliance with food safety regulations as it is consumed by humans.

The existing flour packaging machines are usually imported, which are not readily accessible and affordable for small- and medium-scale farmers or food processing industries in the country (Mogaji *et al.*, 2019). These machines are also hard to be operated, maintained and repaired by people with low technical know-how. Consequently, this has led to the utilization of traditional and unhygienic plantain flour packaging methods, which adversely affect the quality and quantity of the produced flour resulting in food-borne health problems, food poisoning and food-transmission of diseases or even viruses like COVID-19. Additionally, using these methods result in bags of flour that are not properly or tightly sealed, thereby affecting the shelf life, quality and nutritional, esteemed and market value. In total, the harvested plantain losses in Nigeria ranged from 5 to 50% as revealed by recent studies of Morris *et al*. (2019) and Olutomilola (2021).

With the information mentioned previously, there is a need to develop a machine for flour packaging, which could be incorporated into a plant's production line that processes unripe plantain into flour (which is being presently developed in Nigeria) using locally available materials for cost-effectiveness and easy maintenance (Olutomilola, 2019). Thus, the aim of this paper was to design and simulate a simple plantain flour packaging machine based on given parameters and materials.

2. Methodology

2.1 Design Concept of the Flour Packaging Machine

The flour packaging machine is a vertical form-fill and four-seal machine. Its three-dimensional (3-D) modelling and assembling were done using SolidWorks 2016 (Computer Aided Design [CAD] software), as shown in Figure 1. This concept was selected based on the plant's layout or configuration, material flow and desire to take advantage of gravity in material flow. Table 1 shows the materials selected for the machine's components and the reasons for selecting them.

The machine was made up of two major sections: metering and packaging. The metering section, whose function is to weigh and deliver plantain flour into the packaging section, consists of three segments: temporary storage or reservoir, metering or weighing and dispensing chamber. All its component parts were made of stainless steel with a density of 8000 kg/m^3 and yield strength of $1.724x10^8$ N/m^2. The temporary storage is a hopper with both cylindrical and conical geometries helping to hold plantain flour temporarily for metering and packaging. The metering segment, aiding in opening and closing the orifice leading to the temporary storage, consists of an orifice, an orifice-shutter plate, a shutter-guide plate and a 12-volt plunger. The plunger controls the opening and closing action of the metering segment. The weighing and dispensing chamber ensures that accurate or desired quantity of plantain flour is measured and delivered into the packaging section for bagging.

The chamber encompasses measuring container, a container-turner or supporting plate, four guiding pins, a weight sensing plate, a load transducer or sensor, a 12-volt geared wiper motor and two feedback switches. The measuring container serves as a container for the desired quantity of flour to be delivered into the packaging section per unit time. The four guiding pins help to hold the measuring container firmly in position. The container-turner tumbles the measuring container so as to empty its content into the packaging section. It also serves as a platform in which the measuring container sits or rests for proper sensing of flour weight by load sensor. The wiper motor controls the clockwise and anticlockwise movement or tumbling of the measuring container. The two feedback switches send signal to the wiper motor to change motion direction from clockwise to anticlockwise and vice versa. The switches send signal to the metering segment to either close or open the orifice leading to the temporary storage for the flour release.

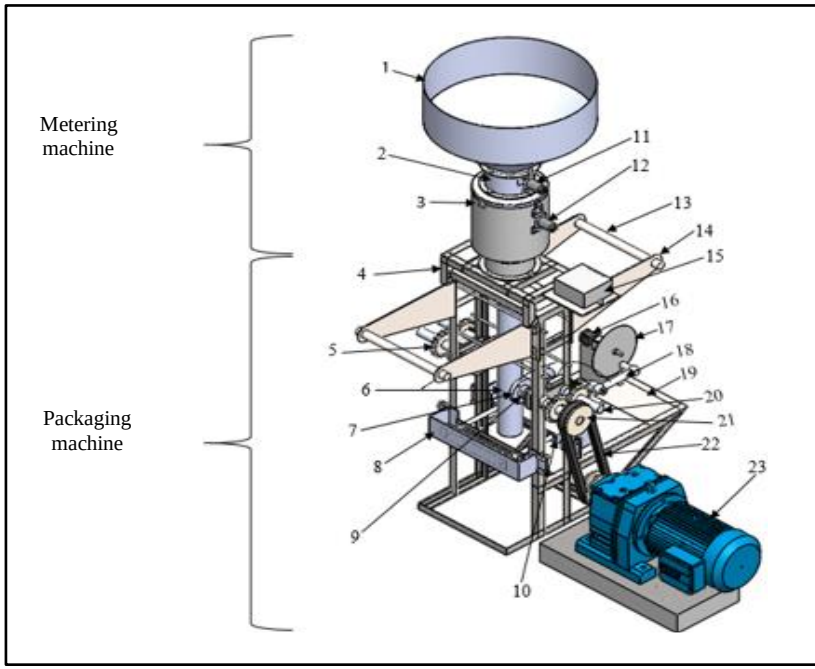

1 – temporary storage; 2 – metering segment; 3 – measuring and dispensing chamber; 4 – frame; 5 – gear drive; 6 – forming and metering pipe; 7 – sealing roller; 8 – rectangular sealer guide and support; 9 – roller heater; 10 – moveable rectangular sealer; 11– plunger; 12 – metering section wiper motor; 13 – nylon roller; 14 – nylon hanger; 15 – control box; 16 – packaging section wiper; 17 – wiper motor disc; 18 – connecting rod; 19 – wiper motor support; 20 – sealing roller shaft; 21 – roller shaft pulley; 22 – V-belt; 23 – gear motor

Figure 1. Isometric view of the metering and packaging machines

Table 1. Material selection for the metering and packaging machine

S/N	Parts	Quantity	Selected Materials	Reasons for Selecting the Materials
1	Temporary storage	1	Stainless steel	Recommended for food processing, Corrosion resistant
2	Metering segment	1	Stainless steel	Recommended for food processing, Corrosion resistant
3	Measuring and dispensing chamber	1	Stainless steel	Recommended for food processing, Corrosion resistant
4	Frame	1	Mild steel	Readily available, low-cost, excellent machinability, strength
5	Gear drive	6	Mild steel	Readily available, low-cost, excellent machinability, strength
6	Forming and metering pipe	1	Stainless steel	Recommended for food processing, Corrosion resistant
7	Sealing roller	4	Stainless steel	Recommended for food processing, Corrosion resistant
8	Rectangular sealer guide and support	2	Mild steel	Readily available, low-cost, excellent machinability, strength
9	Roller heater	4	Not applicable	Not applicable
10	Moveable rectangular sealer	1	Stainless steel	Recommended for food processing, Corrosion resistant
11	Plunger	1	Not applicable	Readily available at low-cost
12	Metering section wiper motor	1	Not applicable	Readily available at low-cost
13	Nylon roller	2	Stainless steel	Recommended for food processing, Corrosion resistant
14	Nylon hanger	4	Stainless steel	Recommended for food processing, Corrosion resistant
15	Control box	1	Wood	Readily available, easy workability, lightness, low-cost
16	Packaging section wiper motor	1	Not applicable	Readily available at low-cost
17	Wiper motor disc	1	Mild steel	Readily available, low-cost, excellent machinability, strength
18	Connecting rod	1	Mild steel	Readily available, low-cost, excellent machinability, strength
19	Wiper motor support	1	Mild steel	Readily available, low-cost, excellent machinability, strength
20	Sealing roller shaft	4	Mild steel	Readily available, low-cost, excellent machinability, strength
21	Roller shaft pulley	1	Mild steel	Readily available, low-cost, excellent machinability, strength
22	V-belt	1	Not applicable	Not applicable
23	Gear motor	1	Not applicable	Excellent speed reduction ratio

The packaging section consists of a frame, a metering and forming pipe, a pair of nylon hangers, two pairs of nylon guides, two pairs of sealing rollers, heaters, a pair of rectangular sealers, a cutter, two compression springs, two servo or wiper motors, a platform (incorporated with jam sensor) for receiving cut bags of plantain flour, a gear motor, a gear and a belt drive. The machine was designed to package a maximum of 1 kg of plantain flour at a time. The frame supports all the component parts of the machine. The forming pipe, located directly beneath the weighing and dispensing chamber of the metering

section, aids in forming the bags for plantain flour while serving as a channel through which plantain flour is introduced into already-formed bags. The two hangers in the machine, located at both sides of the top of the supporting frame, hold the two reams of nylon firmly in position to aid unrolling of nylon for bag-forming.

The nylon guides, situated below nylon hangers and on both sides of the frame, assist the unrolled-nylons from the two reams to remain vertical and parallel to each other for proper forming of packaging bags. Operating with the principle of laminating machine, the sealing rollers below nylon guides pull down the nylon from the two reams. The sealing rollers seal the left and right sides of any soon-to-be-formed bag. The sealing rollers are driven by a gear motor through gear drives. The heaters behind the sealing rollers supply the heat needed for sealing and forming of bags to the sealing rollers.

There are two rectangular sealers below the sealing rollers: one is fixed while the other one is movable. The rectangular sealers seal the bottom of soon-to-be-formed bag and the top of already-formed and filled bag. The fixed rectangular sealer has a rectangular sealing plate directly in its front, which is separated by two compression springs. The springs are directly positioned behind the rectangular sealing plate to allow the cutter to protrude by 10 mm beyond the sealing plate into the movable rectangular sealer. The provision of 10 mm is also made on the movable sealer to accommodate the penetration of the cutter into it. The cutter, separating the bottom of soon-to-be-formed bag from the top of already-formed and filled bag, is located at the center of the fixed rectangular sealer. The linear motion, needed by the movable rectangular sealer to perform its intended function, is provided by a servo or wiper motor.

Since each sealing roller is 120 mm in diameter, one revolution gives a formed, filled and sealed bag of 377 mm high or long while 80 mm diameter gives 251 mm, which is the needed bag's height. Hence, two-thirds of one revolution of the sealing roller is required to produce a bag with a height of 251 mm. The rollers stop rotating after making the revolution, and the wiper motor turns the measuring container allowing plantain flour to be dosed into the formed bag. The orifice-shutter plate is actuated by plunger to close the orifice leading to the temporary storage when preset weight of plantain flour is received by the measuring container. The wiper motor is then actuated to turn and empty the measuring container into already-formed bag through the metering and forming pipe.

The measuring container is made to return to its horizontal position, ready to receive another preset weight of flour through a feedback switch. The whole process is repeated after the measuring container has received another preset weight of plantain flour. Moreover, the movable rectangular sealer (which undergoes reciprocating motion) then moves to seal and cut the formed and filled bag against the fixed cutter. Above and below the cutter are sealers, sealing the top of already filled bag and the bottom of soon-to-be-formed bag. The movable rectangular sealer retreats after a delay time of 5 s based on material flow in the process plant. Immediately, the bag falls off the cutter and rectangular sealers. The movable rectangular sealer completes its retreat, the sealing rollers are automatically actuated to make another revolution and the whole process is repeated.

2.2 Design Analysis of the Metering Section

The temporary storage is a funnel-like structure with three substructures: a large cylinder (designed to hold 17 kg), a truncated cone (intended to hold 8 kg) and a small sized cylinder (known as orifice) as shown in Figure 2.

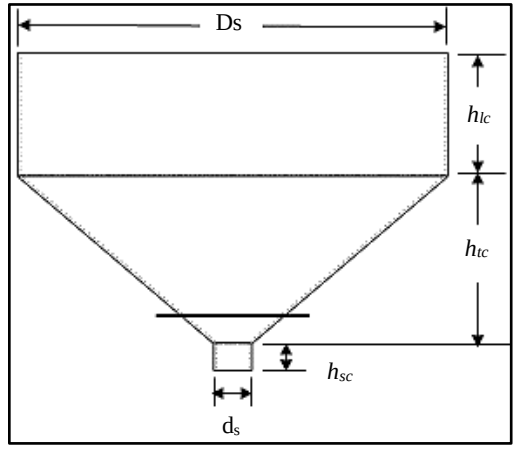

Figure 2. Packaging machine reservoir

The temporary storage or reservoir is expected to hold a maximum of 25 kg of plantain flour at a time since the process plant (which the machine would serve) is expected to produce 1000 kg of flour per day. The height and diameter of the orifice were selected based on available plunger throw, which are 55 and 20 mm, respectively. A 12-volt plunger was selected to close and open the orifice to the temporary storage based on its availability, low power consumption and ability to serve the intended purpose satisfactorily.

Equations 1 to 3 were used to determine the total height of the temporary storage (Khurmi and Gupta, 2008; Macrae *et al.*, 2014).

$$\rho_{pf} = \frac{m_{fts}}{V_{fts}} \tag{1}$$

where ρ_{pf} is the density of plantain flour (200 kg/m^3) (Essien *et al.*, 2016); m_{fts} is the mass of plantain flour in the temporary storage (25 kg); and V_{fts} is the volume of plantain flour in the temporary storage.

2.2.1 Determination of the Heights of Large Cylinder and Truncated Cone

The height of the large cylinder was determined to be 221 mm using Equations 1 and 2.

From Equation 1,

$$V_{lc} = \frac{m_{flc}}{\rho_{pf}} = 0.085\ m^3$$

$$h_{lc} = \frac{V_{lc}}{\pi R_{lc}^2} \tag{2}$$

Since the mass of flour in the truncated cone is 8 kg, the height of the truncated cone was determined as 303 mm using Equation 3. From Equation 1, the volume of the truncated cone was estimated as 0.04 m^3. Hence, the total height of the temporary storage is 579 mm.

$$V_{tc} = \frac{m_{tc}}{\rho_{pf}}$$

$$h_{tc} = \frac{3V_{tc}}{\pi\left(R_{tc}^2 + r_{tc}^2 + R_{tc}r_{tc}\right)} \tag{3}$$

where m_{flc} is the mass of flour in large cylinder (17 kg); V_{lc} is the volume of the large cylinder; R_{lc} is the radius of the large cylinder (0.35 m); h_{lc} is the height of the large cylinder; m_{tc} is the mass of flour in truncated cone; R_{tc} is the radius of larger end of truncated cone (0.35 m); r_{tc} is the radius of smaller end of truncated cone (0.01 m); and h_{tc} is the height of truncated cone.

2.2.2 Shaft Design for the Weighing and Dispensing Chamber

A geared wiper motor of 12 volts was selected to turn the measuring container and its accessories based on its availability, low power consumption and

ability to satisfactorily serve the intended purpose. The measuring container, its supporting plate or turner (2 mm thick), its four guiding pins (1 mm thick), its weight-sensing plate (1 mm thick) and load sensor must be supported and driven by a shaft of adequate strength and rigidity.

The weight of empty measuring container is 200 g and it is expected to receive 1 kg of flour at a time. The total weight of the measuring container, base plate for the measuring container, four guiding pins, weight-sensing plate and weight-sensing rod were calculated as 12, 9, 1, 1.01 and 0.31 N using Equations 4, 5, 6, 7 and 8, respectively. The total weight of base plate for the measuring container was calculated as 9 N using Equation 5. Hence, the total weight of the measuring/dispensing chamber accessories was 23.32 N from Equation 9.

$$W_{TMC} = (m_{MC}+m_{pf})g \tag{4}$$

$$W_{Tbp} = \pi \times r_{bp}^2 \times t_{bp} \times \rho_{ss} \times g \tag{5}$$

$$W_{Tgp} = 4L_{gps} \times w_{gps} \times t_{gps} \times \rho_{ss} \times g \tag{6}$$

$$W_{Twsp} = \pi \times r_{wsp}^2 \times t_{wsp} \times \rho_{ss} \times g \tag{7}$$

$$W_{Twsr} = \pi \times r_{wsr}^2 \times h_{wsr} \times \rho_{ss} \times g \tag{8}$$

$$W_{TMDCA} = W_{TMC} + W_{Tbp} + W_{Tgp} + W_{Twsp} + W_{Twsr} \tag{9}$$

where W_{TMC} is the total weight of the measuring container; m_{MC} is the mass of empty measuring container (0.2 kg); m_{pf} is the mass of plantain flour in the measuring container (1 kg); W_{Tbp} is the total weight of base plate for the measuring container; r_{bp} is the radius of the base plate (135 mm); t_{bp} is the thickness of the base plate (2 mm); ρ_{ss} is the density of stainless steel (8000 kg/m^3); W_{Twsp} is the total weight of weight-sensing plate; r_{wsp} is the radius of weight-sensing plate (64 mm); t_{wsp} is the thickness of weight-sensing plate (1 mm); W_{Twsr} is the total weight of weight-sensing rod; r_{wsr} is the radius of weight-sensing rod (5 mm); h_{wsr} is the height of weight-sensing rod (50 mm); and W_{TMDCA} is the total weight of of the measuring/dispensing chamber accessories.

The load, shear force and bending moment diagram of the measuring/dispensing chamber accessories shaft is shown in Figure 3.

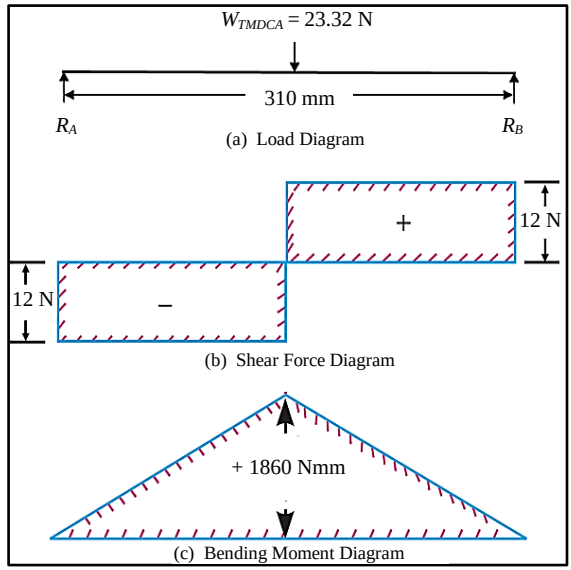

Figure 3. Load, shear force and bending moment diagrams of measuring/dispensing chamber shaft

According to Khurmi (2012) and Rajput (2013), the shaft was treated as simply supported beam with gradually applied point load of 23.32 N, acting at the middle of the beam. Hence, Equation 10 was obtained from Figure 3.

$$R_A = R_B = \frac{(W_{TMDCA})}{2} \approx 12\ N \tag{10}$$

The maximum bending moment was obtained at the midpoint of the shaft as follows: $M_{MDCS}=155R_A=155\times12=1860\ Nmm$. The shaft diameter of the weighing and dispensing chamber was estimated as 14.5 mm using Equation 11. Hence, a shaft diameter of 15 mm was selected to drive the weighing and dispensing chamber accessories.

$$d_{MDCS}=\sqrt[3]{\frac{16\left(\sqrt{(K_m\times M_{MDCS})^2+(K_t\times T_{MDCS})^2}\right)}{\pi\times\tau_{ass}}} \tag{11}$$

where d_{MDCS} is the shaft diameter of the weighing and dispensing chamber; K_m is 1.5; K_t is 1.0; M_{MDCS} is the maximum bending moment; T_{MDCS} is the twisting moment or torque of the wiper motor (25 Nm); and τ_{ass} is the allowable shear stress of the shaft (42 MPa) (Khurmi and Gupta, 2008).

2.3 Design Analysis of the Packaging Section

Since the packaging machine operates with the principle of laminating machine, whose speed ranges from 3 to 15 revolutions per minute (rpm), the sealing rollers' speed was selected to be 9 rpm to achieve a proper seal on the packaging nylon used. The sealing rollers are made of stainless steel whose density is 8000 kg/m^3, with a radius of 60 mm and a thickness of 20 mm. The force required to rotate the sealing rollers and their accessories was calculated as 4.1 N using Equation 12. The mass of individual sealing roller was calculated as 2 kg per Equation 15. Hence, the total mass of the four sealing rollers is 8 kg. It was also assumed that the weight of flour being bagged is equally shared by the four sealing rollers. This weight was added to the total weight of the sealing rollers. A maximum of 10 kg of plantain flour was also assumed for safety reasons so that the rollers will be able to withstand future load increments up to a maximum of 10 kg. Hence, the overall weight of the sealing rollers was assumed to be approximately equal to 20 kg. A weight of 10 kg was also assumed for the shafts on which the rollers and gears are mounted, and to take care of other additional weights.

$$F_{sra} = m_{TD} \times a_{sra} \tag{12}$$

$$a_{sra} = r_{sr} \times \omega_{sra}^2 \approx 0.1 \ \ m/s \tag{13}$$

$$\omega_{sra} = \frac{2\pi N_{sr}}{60} \approx 1 \, rad/sec \tag{14}$$

$$m_{isr} = \pi r_{sr}^2 h_{sr} \rho_{ss} \approx 2 \, kg \tag{15}$$

The total mass of the sealing rollers' gears, which are six in number, was estimated using Equation 16.

$$m_{Tsrg} = 6\left(\pi \times r_{srg}^2 \times t_{srg} \times \rho_{ms}\right) \approx 11 \, kg \tag{16}$$

$$m_{TD} = m_{osr} + m_{Tsrg} + m_{saw} = 41 \, kg \tag{17}$$

The power required to drive the sealing rollers and the power required by gear motor to drive the sealing rollers are given by Equations 18 and 19, respectively. Hence, a gear motor of 1 hp (746 W) was selected for the drive.

$$P_{sra} = F_{sra} \times v_{sr} = F_{sra} \times r_{sr} \times \omega_{sra} = 0.41 \, watt \tag{18}$$

$$P_{Mdsr} = P_{sra} \times P_f \approx 1 \, watt \tag{19}$$

where F_{sra} is the force required to rotate the sealing rollers and their accessories; m_{TD} is the total weight to be driven (kg); a_{sra} is the acceleration of sealing roller (m/s^2); ω_{sra} is the angular velocity of sealing roller; N_{sr} is the number of revolution of the sealing roller (9 rpm); r_{sr} is the radius of sealing roller (0.06 m); m_{isr} is the mass of individual sealing roller (kg); m_{Tsrg} is the total mass of the sealing rollers' gears; r_{srg} is the radius of each sealing roller's gear; t_{srg} is the thickness of each sealing roller's gear; ρ_{ms} is the density of mild steel from which the gears were made (7800 kg/m^3); m_{TD} is the total weight to be driven; m_{osr} is the overall weight of the sealing rollers (20 kg); m_{saw} is the weight of shaft plus other additional weights; a_{sra} is the acceleration of sealing rollers and their accessories; P_{sra} is the power required to drive each sealing roller; v_{sr} is the velocity of sealing rollers; P_{Mdsr} is the power required by gear motor; and P_f is the power factor (2).

2.3.1 Determination of Sealing Roller's Shaft Diameter

The torque transmitted by the shaft was determined to be 791430 Nmm using Equation 20, while the shaft diameter of the sealing roller was calculated as 15 mm using Equation 21 from its space diagram presented in Figure 4. A pulley of equal diameter with the sealing rollers was selected to drive the rollers.

$$T_{ts} = \frac{60 \times P_{tms}}{2\pi N_{sr}} \tag{20}$$

$$d_{sr} = \sqrt[3]{\frac{16\left(\sqrt{(M_s)^2 + (T_{ts})^2}\right)}{\pi \times \tau_s}} \approx 15\ mm \tag{21}$$

where T_{ts} is the torque transmitted by the shaft; P_{tms} is the power transmitted from motor to shaft (746 W); M_s is the bending moment of the shaft; τ_s is the allowable shear stress of the shaft material (42 N/mm^2); and d_{sr} is the diameter of each sealing roller shaft.

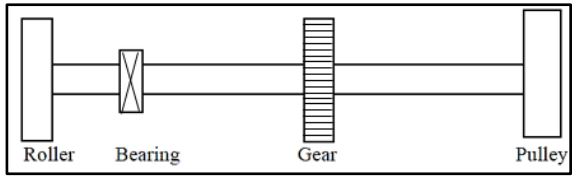

Figure 4. Space diagram of the sealing roller shaft

2.3.2 Determination of Heat Required for Sealing

The temperature required to seal the packaging nylon is 105 °C. The amount of heat required to be transferred to the sealing rollers to affect the sealing action was determined to be 5.904 kJ using Equation 22 (Rajput, 2007). Nichrome wire was adopted as the heating element by considering its properties. The selected heater is a ring type with a diameter, width and thickness of 0.06, 0.02 and 0.005 m, respectively.

$$Q_{hr} = m_h c_{nw} (\theta_2 - \theta_1) \tag{22}$$

$$m_{he} = \rho_n \times V_{he} = 0.160\ kg \tag{23}$$

$$L_{he} = \pi D_{he} = 0.189\ m \tag{24}$$

$$V_{he} = L_{he} \times t_{he} \times w_{he} = 1.89 \times 10^{-5}\ m^3 \tag{25}$$

where Q_{hr} is the heat required to heat up the roller; m_{he} is the heater's mass; c_{nw} is the specific heat capacity of nichrome wire (450 J/kg/K); θ_1 is the heater's initial temperature (23 °C), which is the average room temperature for a production hall; θ_2 is the heater's final temperature (105 °C); ρ_n is the density of nichrome (8400 kg/m^3); V_{he} is the heater's volume; L_{he} is the heater's length before turning into ring (0.06 m); D_{he} is the heater's diameter; t_{he} is the heater's thickness (0.005 m); and w_{he} is the heater's width (0.02m).

2.4 Simulation Study of the Packaging Machine

Following the recommendation of Olutomilola (2021), the workability, functionality and structural stability of the packaging machine's design were evaluated by simulating its developed model using SolidWorks 2016 (CAD software). During which, the properties of the materials selected for the machine were taken into account. In achieving this, models of the machine's major components (reservoir, metering segment, measuring/dispensing chamber, container-turner, frame, forming pipe and sealing roller) were first discretized into 36722 nodes and 17639 elements to generate their solid mesh for finite element analysis (FEA) (Olutomilola, 2019; Olutomilola *et al*., 2020). They were then subjected to load analysis through simulation runs using FEA. During the simulation, the reservoir was subjected to a pressure of 101325 N/m^2; metering segment to a force of 638 N; measuring/dispensing chamber to a force of 700 N and a torque of 70 Nm; container-turner to a pressure of 101325 N/m^2; frame to a force of 700 N; forming pipe to a force

of 100 N as well as acceleration due to gravity of 9.81 m/s^2; and sealing roller to a torque of 450 Nm. The areas where induced stress, static displacement and static strain were significant on their finite element models (FEMs) were noted and designated as A, B and C, respectively, as shown in Figures 5 to 11. The results obtained from the evaluation were then tabulated.

3. Results and Discussion

3.1 Design Evaluation of Metering Section Model

Results of the reservoir's stress, static displacement and strain analysis are presented in Figure 5 and Table 2, respectively. It can be seen that the induced stress (5.227x10^7 N/m^2), static displacement (0.1181 mm) and strain (2.132x10^{-4}) are at maximum level and evenly distributed towards the conical end or reservoir's base. This is attributed to the concentration of the entire weight/pressure of flour and the reservoir in that portion of the structure. This means that the more conical the portion is, the higher the induced stress will be. However, the induced stress was observed to be acceptably below the yield strength (1.724x10^8 N/m^2) of the selected stainless steel as evidenced by factor of safety (FOS) value of 3.4.

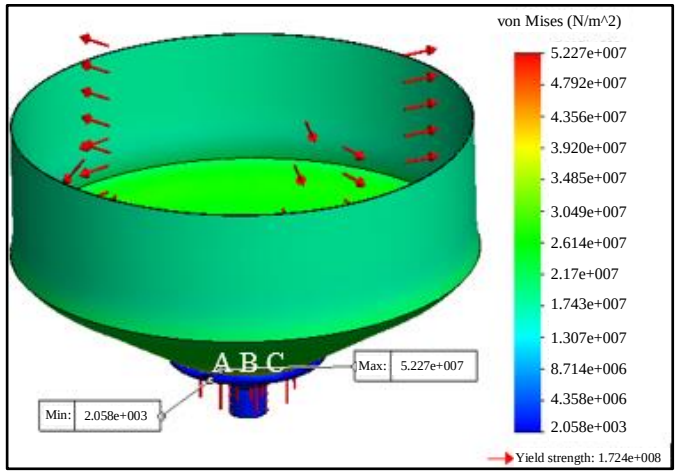

Figure 5. FEM of stress distributions on the reservoir

Table 2. Simulation results of the reservoir

S/N	Stress distributions (N/m^2)	Static displacement (mm)	Static strain	FOS
1	5.227×10^{7}	1.181×10^{-1}	2.132×10^{-4}	3.398
2	4.792×10^{7}	1.082×10^{-1}	1.954×10^{-4}	6.983×10^{3}
3	4.356×10^{7}	9.840×10^{-1}	1.776×10^{-4}	1.396×10^{4}
4	3.920×10^{7}	8.856×10^{-2}	1.599×10^{-4}	2.094×10^{4}
5	3.485×10^{7}	7.872×10^{-2}	1.421×10^{-4}	2.792×10^{4}
6	3.049×10^{7}	6.888×10^{-2}	1.244×10^{-4}	3.490×10^{4}
7	2.614×10^{7}	5.904×10^{-2}	1.066×10^{-4}	4.188×10^{4}
8	2.178×10^{7}	4.920×10^{-2}	8.883×10^{-5}	4.886×10^{4}
9	1.743×10^{7}	3.936×10^{-2}	7.107×10^{-5}	5.584×10^{4}
10	1.307×10^{7}	2.952×10^{-2}	5.330×10^{-5}	6.282×10^{4}
11	8.714×10^{6}	1.968×10^{-2}	3.554×10^{-5}	6.980×10^{4}
12	4.358×10^{6}	9.840×10^{-3}	1.778×10^{-5}	7.678×10^{4}
13	2.058×10^{3}	1.000×10^{-3}	1.288×10^{-8}	8.375×10^{4}

Figure 6 and Table 3 present the stress distribution and simulation results of the metering segment, respectively. The induced stress was observed to be at the maximum level ($8.618x10^{7}$ N/m^2) at the upper flange of the structure, which could be due to the flange supporting the weight of the reservoir and its contents (plantain flour). The static displacement was at the maximum level (0.1057 mm) at the shutter's guides of the metering plate at the center of the structure, while static strain was observed to be at the maximum level ($2.394x10^{-4}$) at the point where the plate is welded to the metering segment. However, it was noted that the induced stress was below the yield strength ($1.724x10^{8}$ N/m^2) of the stainless steel selected for the structure with FOS of 2.0.

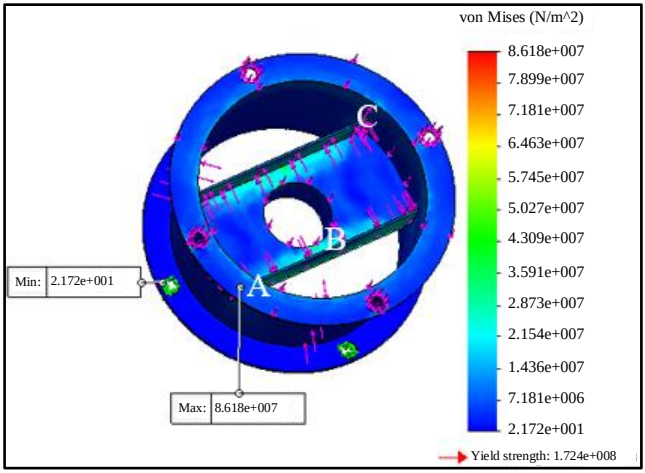

Figure 6. FEM of stress distribution within the metering segment members

Table 3. Simulation results of the metering segment

S/N	Stress distributions (N/m^2)	Static displacement (mm)	Static strain	FOS
1	8.618×10^{7}	1.057×10^{-1}	2.394×10^{-4}	2.000
2	7.899×10^{7}	9.689×10^{-2}	2.195×10^{-4}	6.612×10^{5}
3	7.181×10^{7}	8.808×10^{-2}	1.995×10^{-4}	1.322×10^{6}
4	6.463×10^{7}	7.928×10^{-2}	1.796×10^{-4}	1.984×10^{6}
5	5.745×10^{7}	7.047×10^{-2}	1.596×10^{-4}	2.645×10^{6}
6	5.027×10^{7}	6.166×10^{-2}	1.397×10^{-4}	3.306×10^{6}
7	4.309×10^{7}	5.285×10^{-2}	1.197×10^{-4}	3.967×10^{6}
8	3.591×10^{7}	4.404×10^{-2}	9.977×10^{-5}	4.629×10^{6}
9	2.873×10^{7}	3.523×10^{-2}	7.981×10^{-5}	5.290×10^{6}
10	2.154×10^{7}	2.643×10^{-2}	5.986×10^{-5}	5.951×10^{6}
11	1.436×10^{7}	1.762×10^{-2}	3.991×10^{-5}	6.612×10^{6}
12	7.181×10^{6}	8.808×10^{-3}	1.996×10^{-5}	7.274×10^{6}
13	2.172×10^{1}	0	1.984×10^{-9}	7.935×10^{6}

As evidenced by the simulation results of the measuring/dispensing chamber presented in Figure 7 and Table 4, the induced stress ($4.17x10^{7}$ N/m^2) and static strain ($1.399x10^{-4}$) were at the maximum level at the point where the tapered end of the chamber is welded to another structure – just the same way it happened in the reservoir. The static displacement was also observed at the maximum level at the periphery of the upper end of the chamber. However, the induced stress value was still below the yield strength ($1.724x10^{8}$ N/m^2) of the stainless steel selected for the chamber.

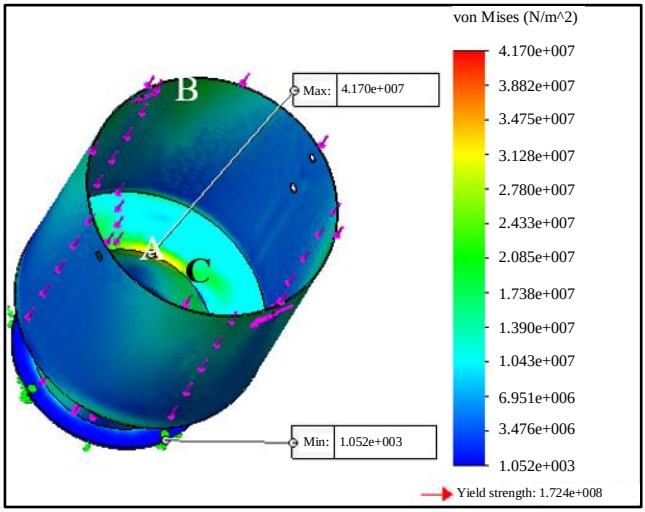

Figure 7. FEM of stress distribution on the measuring/dispensing chamber

Table 4. Simulation results of the measuring/dispensing chamber

S/N	Stress distributions (N/m^2)	Static displacement (mm)	Static strain	FOS
1	4.170×10^{7}	0.9154	1.399×10^{-4}	4.134
2	3.822×10^{7}	0.8391	1.282×10^{-4}	1.366×10^{4}
3	3.475×10^{7}	0.7629	1.166×10^{-4}	2.731×10^{4}
4	3.128×10^{7}	0.6866	1.049×10^{-4}	4.097×10^{4}
5	2.780×10^{7}	0.6103	9.325×10^{-5}	5.462×10^{4}
6	2.433×10^{7}	0.5340	8.160×10^{-5}	6.827×10^{4}
7	2.085×10^{7}	0.4577	6.994×10^{-5}	8.193×10^{4}
8	1.738×10^{7}	0.3814	5.829×10^{-5}	9.558×10^{4}
9	1.390×10^{7}	0.3051	4.663×10^{-5}	1.092×10^{5}
10	1.043×10^{7}	0.2289	3.497×10^{-5}	1.229×10^{5}
11	6.951×10^{6}	0.1526	2.332×10^{-5}	1.365×10^{5}
12	3.476×10^{6}	0.0763	1.166×10^{-5}	1.502×10^{5}
13	1.052×10^{3}	1.000×10^{-30}	5.561×10^{-9}	1.639×10^{5}

The results of the container-turner's FEA are shown in Figure 8 and Table 5. It can be seen that the maximum induced stress ($9.018\text{x}10^{7}$ N/m^2), static displacement ($8.582\text{x}10^{-3}$ mm) and strain ($3.015\text{x}10^{-4}$) were located and evenly distributed at the points where the turning shaft is joined to the container-turner. This is caused by the concentration of weights of the structure and its accessories on the two points. The maximum induced stress was still acceptably below the yield strength ($1.724\text{x}10^{8}$ N/m^2) of the stainless steel selected with FOS of 1.9. Thus, the shaft diameter must be carefully monitored during fabrication to prevent sagging.

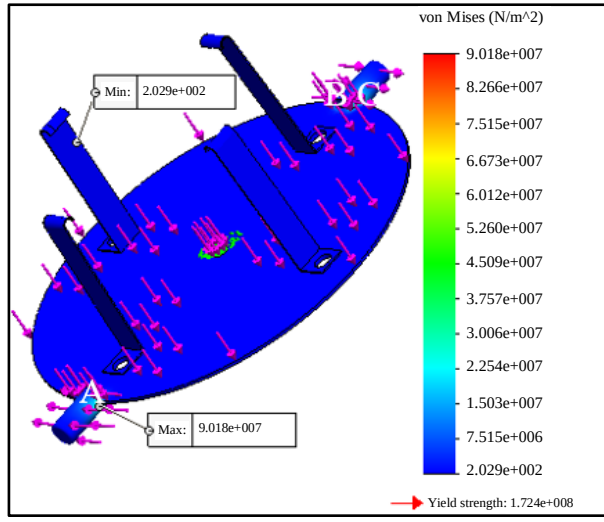

Figure 8. FEM of stress distribution within the container-turner

Table 5. Simulation results of the container-turner

S/N	Stress distributions (N/m^2)	Static displacement (mm)	Static strain	FOS
1	9.018×10^{7}	8.582×10^{-3}	3.015×10^{-4}	1.911
2	8.266×10^{7}	7.867×10^{-3}	2.764×10^{-4}	7.080×10^{8}
3	7.515×10^{7}	7.152×10^{-3}	2.512×10^{-4}	1.416×10^{9}
4	6.763×10^{7}	6.437×10^{-3}	2.261×10^{-4}	2.124×10^{9}
5	6.012×10^{7}	5.722×10^{-3}	2.010×10^{-4}	2.832×10^{9}
6	5.260×10^{7}	5.006×10^{-3}	1.759×10^{-4}	3.540×10^{9}
7	4.509×10^{7}	4.291×10^{-3}	1.507×10^{-4}	4.248×10^{9}
8	3.757×10^{7}	3.576×10^{-3}	1.256×10^{-4}	4.956×10^{9}
9	3.006×10^{7}	2.861×10^{-3}	1.005×10^{-4}	5.664×10^{9}
10	2.254×10^{7}	2.146×10^{-3}	7.537×10^{-5}	6.372×10^{9}
11	1.503×10^{7}	1.430×10^{-3}	5.025×10^{-5}	7.080×10^{9}
12	7.515×10^{6}	7.152×10^{-4}	2.512×10^{-5}	7.788×10^{9}
13	2.029×10^{-2}	1.000×10^{-30}	6.587×10^{-14}	8.496×10^{9}

The minimum FOS values obtained from the FEA of the reservoir, metering segment, measuring/dispensing chamber and container-turner of the metering machine were 3.3, 2, 4.1 and 1.9, respectively. However, the maximum stress values obtained from FEA were acceptably lower than the yield strength value of the stainless steel selected for their fabrication as previously mentioned. Hence, the simulation results of the whole metering section attest that failure may not likely occur since the minimum FOS value obtained so far was 1.9, which is sufficient enough to prevent the component parts of the machine from experiencing structural failures during service under normal working conditions (Olutomilola *et al*., 2020). However, the locations with the highest induced-stresses must be considered and reinforced for optimum performance since they are potential areas where failure may likely begin after a long period of use (Olutomilola *et al*., 2019).

3.2 Design Evaluation of Packaging Section Model

Figure 9 and Table 6 present the results of the FEA conducted on the machine's frame. The maximum induced stress ($1.482x10^{8}$ N/m^2), static displacement (11.7 mm) and static strain ($8.941x10^{-5}$) obtained were observed to be located at welded joints (directly located above the nylon hangers). The static displacement was very high while the induced stress was not too far below the yield strength ($2.482x10^{8}$ N/m^2) of the mild steel selected for the frame with an FOS of 1.7. This is linked to the joints supporting the weight of the metering section, its accessories and contents.

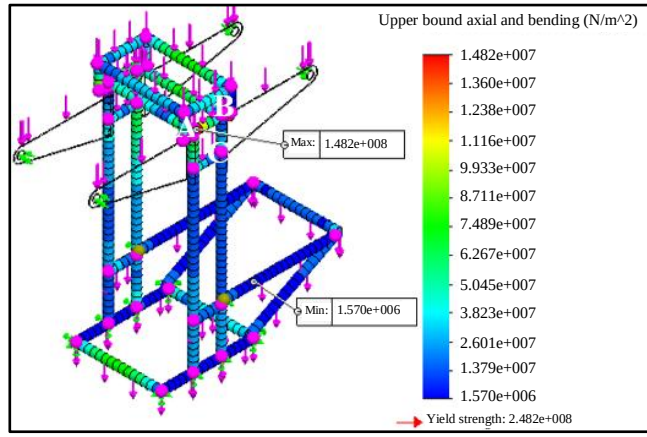

Figure 9. FEM of stress distribution within machine frame members

Table 6. Simulation results of the machine frame

S/N	Stress distributions (N/m^2)	Static displacement (mm)	Static strain	FOS
1	1.482×10^{8}	11.700	8.941×10^{-5}	1.674
2	1.360×10^{8}	10.720	8.196×10^{-5}	1.129×10^{3}
3	1.238×10^{8}	9.750	7.451×10^{-5}	2.256×10^{3}
4	1.116×10^{8}	8.775	6.706×10^{-5}	3.383×10^{3}
5	9.933×10^{7}	7.800	5.961×10^{-5}	4.510×10^{3}
6	8.711×10^{7}	6.825	5.216×10^{-5}	5.637×10^{3}
7	7.489×10^{7}	5.850	4.470×10^{-5}	6.764×10^{3}
8	6.267×10^{7}	4.875	3.725×10^{-5}	7.891×10^{3}
9	5.045×10^{7}	3.900	2.980×10^{-5}	9.018×10^{3}
10	3.823×10^{7}	2.925	2.235×10^{-5}	1.015×10^{4}
11	2.601×10^{7}	1.950	1.490×10^{-5}	1.127×10^{4}
12	1.379×10^{7}	9.750	7.451×10^{-6}	1.240×10^{4}
13	1.570×10^{6}	1.000×10^{-30}	0	1.353×10^{4}

The results of the simulation carried out on the forming pipe are as shown in Figure 10 and Table 7. The induced stress and static strain were at the maximum level at the point where the flange is welded to the forming pipe. Similarly, static displacement was at the maximum level at the exit end of the nylon-forming pipe. However, the induced stress ($1.931x10^7$ N/m^2) was far below the yield strength ($1.724x10^8$ N/m^2) of the selected stainless steel.

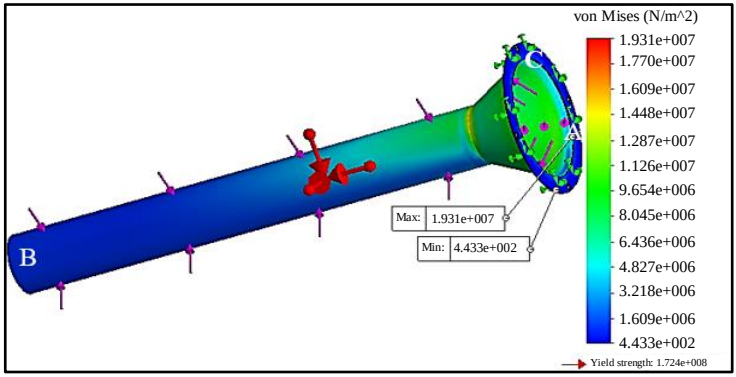

Figure 10. FEM of stress distribution on the forming pipe

Table 7. Simulation results of the forming pipe

S/N	Stress distributions (N/m^2)	Static displacement (mm)	Static strain	FOS
1	1.931×10^{7}	0.2249	1.146×10^{-4}	8.927
2	1.770×10^{7}	0.2062	1.050×10^{-4}	3.241×10^{4}
3	1.609×10^{7}	0.1874	9.549×10^{-5}	6.481×10^{4}
4	1.448×10^{7}	0.1687	8.594×10^{-5}	9.721×10^{4}
5	1.287×10^{7}	0.1499	7.639×10^{-5}	1.296×10^{5}
6	1.126×10^{7}	0.1312	6.684×10^{-5}	1.620×10^{5}
7	9.654×10^{6}	0.1124	5.729×10^{-5}	1.944×10^{5}
8	8.045×10^{6}	9.371×10^{-2}	4.775×10^{-5}	2.268×10^{5}
9	6.436×10^{6}	7.497×10^{-2}	3.820×10^{-5}	2.592×10^{5}
10	4.827×10^{6}	5.622×10^{-2}	2.865×10^{-5}	2.916×10^{5}
11	3.218×10^{6}	3.748×10^{-2}	1.910×10^{-5}	3.240×10^{5}
12	1.609×10^{6}	1.874×10^{-2}	9.550×10^{-6}	3.564×10^{5}
13	4.433×10^{2}	1.000×10^{-30}	1.238×10^{-9}	3.888×10^{5}

The results of sealing roller's simulation (Figure 11 and Table 8) show that the highest induced stress ($9.2281x10^{7}$ N/m^2) and static strain ($3.477x10^{-4}$) obtained were evenly distributed at the point where the shaft is joined with the roller. The maximum static displacement was also evenly dispersed at the pulley-bearing end of the roller shaft. However, the induced stress fell below the yield strength ($2.482x10^{8}$ N/m^2) of the mild steel selected for the sealing roller with an FOS of 2.4.

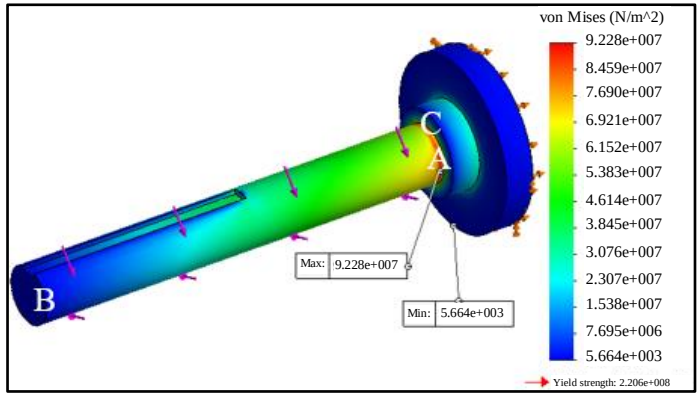

Figure 11. FEM of stress distribution on the sealing roller

Table 8. Simulation results of the sealing roller

S/N	Stress distributions (N/m^2)	Static displacement (mm)	Static strain	FOS
1	9.2281×10^{7}	0.3619	3.477×10^{-4}	2.391
2	8.459×10^{7}	0.3317	3.188×10^{-4}	3.248×10^{3}
3	7.690×10^{7}	0.3016	2.898×10^{-4}	6.493×10^{3}
4	6.921×10^{7}	0.2714	2.609×10^{-4}	9.738×10^{3}
5	6.152×10^{7}	0.2413	2.319×10^{-4}	1.298×10^{4}
6	5.383×10^{7}	0.2111	2.030×10^{-4}	1.623×10^{4}
7	4.614×10^{7}	0.1810	1.740×10^{-4}	1.947×10^{4}
8	3.845×10^{7}	0.1508	1.451×10^{-4}	2.272×10^{4}
9	3.076×10^{7}	0.1206	1.161×10^{-4}	2.597×10^{4}
10	2.307×10^{7}	9.048×10^{-2}	8.718×10^{-5}	2.921×10^{4}
11	1.538×10^{7}	6.032×10^{-2}	5.824×10^{-5}	3.246×10^{4}
12	7.695×10^{6}	3.016×10^{-2}	2.929×10^{-5}	3.570×10^{4}
13	5.664×10^{3}	1.000×10^{-30}	3.404×10^{-7}	3.895×10^{4}

The obtained FEA results implied that the packaging machine, when fabricated, will be able to satisfactorily perform its intended functions under normal working conditions since the maximum stress values obtained from the FEA of its components were far lower than the corresponding yield strength values of the materials selected for fabrication (Olutomilola *et al*., 2019). However, the points that were subjected to these stress values may be potential areas where failure may likely begin after a long time of use. However, failure may not likely occur since the FOS values obtained for critical components were high enough to prevent the machine from

experiencing structural failures under normal working conditions (Olutomilola and Omoaka, 2018). Thus, it can be inferred that the packaging machine's design is adequate and safe for fabrication. If necessary, the materials selected for the machine could be reviewed to further increase or reduce the obtained FOS values (Olutomilola *et al*., 2020).

4. Conclusion and Recommendation

In this study, a flour packaging machine has been designed for a plant's production line that processes unripe plantain into flour. Its functionality and structural reliability were evaluated by simulation, and its design was found to be adequate and safe for fabrication as evidenced by the results obtained from the FEA of the developed model. This establishes the machine's ability to serve its intended purpose when fabricated and incorporated into the plant. Although, the machine is believed not to fail during service by virtue of the FOS values obtained from its FEA, the locations with the maximum induced-stresses are potential areas where failure may probably be initiated after a long period of time in service. Thus, there is a need to pay keen attention to the said locations during fabrication and care must be taken to reinforce them (if necessary) for optimum reliability of the machine.

This study is expected to serve as a guide for the development of packaging machines for processing Nigerian agricultural produce using locally or readily available materials, tools, manufacturing technologies and discarded-components of automobiles or electrical appliances (such as wiper motors, plungers, etc.) as a way of turning waste into wealth.

5. Acknowledgement

Tertiary Education Trust Fund (TETFund) Nigeria is acknowledged for the financial support, research grant ref: VCPU/TETFund/155. The Advanced Manufacturing and Applied Ergonomics Research Team (AMAERT), Abegunde Ademola S., Ihinmoyan Ifeoluwa Moses, Ijete Oluwatobi Godswill and Beremoye Adeoye Samuel contributed towards the success of this research work.

6. References

Adeyeri, M.K., Ayodeji, S.P., Olutomilola, E.O., & Bako, J.O. (2020). Design of a Screw Conveyor for Transporting and Cooling Plantain Flour in a Process Plant. Jordan Journal of Mechanical and Industrial Engineering, 14(4), 425-436.

Alonso-Gomez, L.A., Solarte-Toro, J.C., Bello-Perez, L.A., & Cardona-Alzate, C.A. (2020). Performance evaluation and economic analysis of the bioethanol and flour production using rejected unripe plantain fruits (*Musa paradisiaca* L.) as raw material. Food and Bioproducts Processing, 121, 29-42. https://doi.org/10.1016/j.fbp.2020.01.005

Ayodeji, S.P. (2016). Conceptual design of a process plant for the production of plantain flour. Cogent Engineering, Production and Manufacturing Research Article, 3, 1-16. https://doi.org/10.1080/23311916.2016.1191743

Eleazu, C.O., & Okafor, P. (2015). Use of unripe plantain (*Musa paradisiaca*) in the management of diabetes and hepatic dysfunction in streptozotocin induced diabetes in rats. Interventional Medicine and Applied Science, 7(1), 9-16. https://doi.org/10.1556/IMAS.7.2015.1.2

Essien, I.E., Antia, A.D., Etuk, S.E., Peter, I.G., & Udofia, A.E. (2016). Investigation of thermal properties of plantain (*Musa paradisiaca*) and Mfang Aya (*Thaumatococcus daniellii*) as thermal radiation insulator. Journal of Natural Sciences Research, 6(15), 33-37.

Fadimu, G.J., Sanni, L.O., Adebowale, A.A., Sobukola, O.P., Abdulsalam-Saghir, P.B., Rasaq, S.A., & Adenekan, M.K. (2019). Effect of drying methods on the sorption isotherms of plantain flour. Croatian Journal of Food Science and Technology, 11(2), 149-156. https://doi.org/10.17508/CJFST.2019.11.2.01

Hussain, A., Bhowmik, B., & Moreira, N.C.D.V. (2020). COVID-19 and diabetes: Knowledge in progress. Diabetes Research and Clinical Practice, 108142(162), 1-9. https://doi.org/10.1016/j.diabres.2020.108142

Khurmi, R.S. (2012). Strength of Materials (mechanics of solids) (23rd ed.). Ram Nagar, New Delhi, India: S. Chand and Company Pvt. Ltd.

Khurmi, R.S., & Gupta, J.K. (2008). A textbook of machine design (1st. multicolour ed.). Ram Nagar, New Delhi, India: Eurasia Publishing House (PVT.) Ltd.

Kouame, C.A., Kouassi, N.K., Abodo, J.R., Pereko, K.K.A., Casiraghi, M.C., N'dri, D.Y., & Amani, G.N. (2017). Glycemic responses, glycemic index, and glycemic load values of some street foods prepared from plantain (Musa spp., AAB Genome) in Côte d'Ivoire. Foods, 6(9), 83. https://doi.org/10.3390/foods6090083.

Macrae, M.F., Chima, Z.I., Garba, G.U., Ademosu, M.O., Kalejaiye, A.O., Channon, J.B., Smith, A.M., & Head, H.C. (2014). New general mathematics for senior secondary schools 1 (4th ed.). Lagos, Nigeria: Pearson Education Limited.

Mogaji, P.B., Ayodeji, S.P., Adeyeri, M.K., Beremoye, A.S., & Olutomilola, E.O. (2019). Design, fabrication and evaluation of a metering system for flour packaging in a plantain process plant. In: Adekunle, A.A., Adejuyigbe, S.B., Arowolo, M.O., Oyelami, A.T., Afolalu, S.A., Martins, O.O. (Eds.), Proceedings of 1st International Mechatronics Engineering Conference, Oye Ekiti, Ekiti State, Nigeria, 52-65.

Morris, K.J., Kamarulzaman, N.H., & Morris, K.I. (2019). Small-scale postharvest practices among plantain farmers and traders: A potential for reducing losses in rivers state, Nigeria. Scientific African, 4, 1-10. https://doi.org/10.1016/j.sciaf.2019.e00086

Olanrewaju, A.S., & Abidemi J.O. (2017). Drying characteristics and thermal properties of two local varieties of unripe plantain. American Journal of Science and Technology, 4(5), 74-79.

Olutomilola, E.O. (2019). Development of a process plant for plantain flour production (Dissertation). Federal University of Technology, Akure, Ondo State, Nigeria.

Olutomilola, E.O. (2021). A review of raw plantain size reduction. Scientific African, 12, 1-15. https://doi.org/10.1016/j.sciaf.2021.e00773

Olutomilola, E.O., & Omoaka, A. (2018). Theoretical design of a plantain peeling machine. FUTA Journal of Engineering and Engineering Technology, 12(2), 229-237.

Olutomilola, E.O., Ayodeji, S.P., & Adeyeri, M.K. (2019). Finite element analysis of a washing and preheating unit designed for plantain flour process plant. International Journal of Engineering Technologies, 5(4), 117-127.

Olutomilola, E.O., Ayodeji, S.P., & Adeyeri, M.K. (2020). Design and Structural Analysis of a Particulating Machine for Plantain Flour Process Plant. ARPN Journal of Engineering and Applied Sciences, 15(17), 1816-1824.

Oluwajuyitan, T.D., & Ijarotimi, O.S. (2019). Nutritional, antioxidant, glycaemic index and antihyperglycaemic properties of improved traditional plantain-based (*Musa AAB*) dough meal enriched with tigernut (*Cyperus esculentus*) and defatted soybean (*Glycine max*) flour for diabetic patients. Heliyon, 5, 1-27. https://doi.org/10.1016/j.heliyon.2019.e01504

Rajput, R.K. (2007). Engineering Thermodynamics (3rd ed.). Daryaganj, New Delhi, India: Laxmi Publications (P) Ltd.

Rajput, R.K. (2013). Strength of Materials (Mechanics of Solids) (5th ed.). Ram Nagar, New Delhi, India: S. Chand and Company Pvt. Ltd.

Seewoodhary, J., & Oozageer, R. (2020). Coronavirus and Diabetes: An update. Practical Diabetes, 37(2), 41-42. https://doi.org/10.1002/pdi.2260

Singh, A.K., Gupta, R., Ghosh, A., & Misra, A. (2020). Diabetes in COVID-19: Prevalence, pathophysiology, prognosis and practical considerations. Diabetes & Metabolic Syndrome: Clinical Research & Reviews, 14, 303-310. https://doi.org/10.1016/j.dsx.2020.04.004

Wang, A., Zhao, W., Xu, Z., & Gu, J. (2020). Timely blood glucose management for the outbreak of 2019 novel coronavirus disease (COVID-19) is urgently needed. Diabetes Research and Clinical Practice, 108118B (162), 1-2. https://doi.org/10.1016/j.diabres.2020.1081184